Evaluation of Matrix9 silicon photomultiplier array for small-animal PET

Junwei Du,[a] Jeffrey P. Schmall, Yongfeng Yang, Kun Di, Emilie Roncali,
and Gregory S. Mitchell
*Department of Biomedical Engineering, University of California-Davis, One Shields Avenue,
Davis, California 95616*

Steve Buckley and Carl Jackson
SensL Technologies Ltd., 6800 Airport Business Park, Cork, Ireland

Simon R. Cherry
*Department of Biomedical Engineering, University of California-Davis, One Shields Avenue,
Davis, California, 95616*

(Received 25 August 2014; revised 4 December 2014; accepted for publication 8 December 2014;
published 12 January 2015)

Purpose: The MatrixSL-9-30035-OEM (Matrix9) from SensL is a large-area silicon photomultiplier (SiPM) photodetector module consisting of a 3×3 array of 4×4 element SiPM arrays (total of 144 SiPM pixels) and incorporates SensL's front-end electronics board and coincidence board. Each SiPM pixel measures 3.16×3.16 mm^2 and the total size of the detector head is 47.8×46.3 mm^2. Using 8×8 polished LSO/LYSO arrays (pitch 1.5 mm) the performance of this detector system (SiPM array and readout electronics) was evaluated with a view for its eventual use in small-animal positron emission tomography (PET).

Methods: Measurements of noise, signal, signal-to-noise ratio, energy resolution, flood histogram quality, timing resolution, and array trigger error were obtained at different bias voltages (28.0–32.5 V in 0.5 V intervals) and at different temperatures (5 °C–25 °C in 5 °C degree steps) to find the optimal operating conditions.

Results: The best measured signal-to-noise ratio and flood histogram quality for 511 keV gamma photons were obtained at a bias voltage of 30.0 V and a temperature of 5 °C. The energy resolution and timing resolution under these conditions were 14.2% ± 0.1% and 4.2 ± 0.1 ns, respectively. The flood histograms show that all the crystals in the 1.5 mm pitch LSO array can be clearly identified and that smaller crystal pitches can also be resolved. Flood histogram quality was also calculated using different center of gravity based positioning algorithms. Improved and more robust results were achieved using the local 9 pixels for positioning along with an energy offset calibration. To evaluate the front-end detector readout, and multiplexing efficiency, an array trigger error metric is introduced and measured at different lower energy thresholds. Using a lower energy threshold greater than 150 keV effectively eliminates any mispositioning between SiPM arrays.

Conclusions: In summary, the Matrix9 detector system can resolve high-resolution scintillator arrays common in small-animal PET with adequate energy resolution and timing resolution over a large detector area. The modular design of the Matrix9 detector allows it to be used as a building block for simple, low channel-count, yet high performance, small animal PET or PET/MRI systems. [http://dx.doi.org/10.1118/1.4905088]

Key words: PET, silicon photomultiplier, Matrix9, nuclear imaging, instrumentation

1. INTRODUCTION

Silicon photomultiplier (SiPM) detectors, also referred to as multipixel photon counters (MPPCs), are attracting significant attention in nuclear imaging, especially for positron emission tomography (PET) applications[1,2] due to their potential for high photodetection efficiency (PDE),[3,4] low working bias voltage, compact size, and insensitivity to magnetic fields which makes them a promising candidate detector to build PET or PET/MR systems. Single channel SiPM detectors, coupled one-to-one to scintillation crystals, have rapidly demonstrated the potential of SiPM-based PET scanners.[5,6] Recently there has been significant academic and industrial development of large area multichannel SiPM technologies[7–20] giving rise to many SiPM-based detector and scanner designs. Besides developing new high performance devices, large-area SiPM modules are also being developed, and some of these modules now include the readout electronics to facilitate the fabrication of PET scanners.[16,20,21] Two different types of SiPM detector designs are of particular interest: pixel array silicon photomultipliers, which already have been used in PET scanner prototypes,[22–25] and position-sensitive silicon photomultipliers.[10,14,26,27] Large area position-sensitive detectors using a build-in resistor grid method or other method to connect each cell in the device require only five readout channels, four for positioning and one for timing,[10,14,26,27] making the electronic readout relatively simple. However, the spatial and timing resolution performance of large-area devices is currently limited, in part because of the high dark count rate, and also their high capacitance.[28] The pixel array detector is the standard SiPM implementation and is based on a large number of separate single SiPM pixels located on the same substrate or printed circuit board (PCB). The advantage of the pixel array detector is that 1:1 coupling is possible (minimizing detector decoding errors), and each individual SiPM pixel provides excellent timing.[20,29,30] However, at the system level many electronic readout channels will be needed if each pixel is read out individually or a complex ASIC is needed. Hence, some channel multiplexing methods are normally used to reduce the number of readout channels and therefore the cost and complexity of a PET scanner based on this architecture.[31–35] This multiplexing will, however, also degrade the detector performance.

SensL's Matrix9 is a modular, large-area SiPM array detector, which includes the detector head (SiPM arrays), frond-end board (amplification, multiplexing, and digitization), coincidence board, and data acquisition and readout software. A "scrambled crosswire readout" technique (see Sec. 2.B) is used to read out the 144 SiPM pixel signals using just 25 electronic channels, including 16 channels for energy and timing, and 9 channels to identify which SiPM array has fired.

Given the flexibility and ease-of-implementation of the Matrix9 we are planning a simple, high-sensitivity, box geometry, small animal PET scanner based on this detector system, motivated by the success of a similar geometry PMT-based system.[36] The purpose of this study was to assess the performance of the Matrix9 detector when using scintillator array dimensions consistent with small-animal PET applications that require light sharing across SiPM pixels to achieve competitive spatial resolution. To find the best operating conditions, the noise, signal, signal-to-noise ratio (SNR), energy resolution, flood histograms quality, timing resolution, and array trigger error ratio of the Matrix9 were measured and compared at five different temperatures, ranging from 5 °C to 25 °C, in 5 °C intervals. Performance at temperatures lower than 5 °C were not studied because the goal was to stay in a temperature range that can be readily and reliably achieved when implemented in a PET scanner. Measurements were also obtained at different bias voltages (~28.0–32.5 V, in 0.5 V increments) to determine the optimum operating bias voltage for the system.

2. MATERIAL AND METHODS

2.A. Matrix9 detector head and crystal arrays

A photograph of the Matrix9 detector head (MatrixSL-9-30035-OEM) is shown in Fig. 1. The detector head consists of a 3×3 matrix of SiPM arrays, each with 4×4 SiPM pixels, for a total of 144 SiPM pixels. The total area of the detector head is 47.8×46.3 mm^2. Each SiPM pixel measures 3.17×3.17 mm^2 and contains 4774 microcells that are each 35×35 μm. The PDE is 14% at 2.0 V above the breakdown voltage of 27.5 V.[37] The surface of the SiPM array was covered by ~0.5 mm thick epoxy glass. The dead space between each SiPM pixel in the same SiPM array is 0.2 mm and the dead space between each SiPM array in the x and y directions are 2.22 and 2.75 mm, respectively. A single bias voltage is applied to all 144 SiPM pixels on the detector head. The pixels in a Matrix9 detector head are preselected to give a uniformity within ±10%.

A front-end board (MatrixSL-9-30035) was connected to the Matrix9 detector head. A scrambled crosswire readout technique (described in Sec. 2.B) is used to read out the 144 SiPM pixel signals using just 25 electronic channels, including 16 channels for energy and timing, and 9 channels to identify which SiPM array has fired. Each front-end board can support one detector head and the coincidence board (Matrix-EVB-16) can support up to 16 individual detector modules. Two Matrix9 detector heads were used in coincidence for the timing measurements, all other measurements used a single Matrix9 detector head.[21]

Two 8×8 polished LSO arrays, with a pitch of 1.5 mm and length 6 mm, separated by enhanced specular reflector (ESR), were used in all measurements except the count rate measurements. For each Matrix9 detector, an LSO array was coupled to the central SiPM array via BC-630 optical grease; the other eight SiPM arrays in the Matrix9 detector were covered with black paper, while all nine SiPM array were

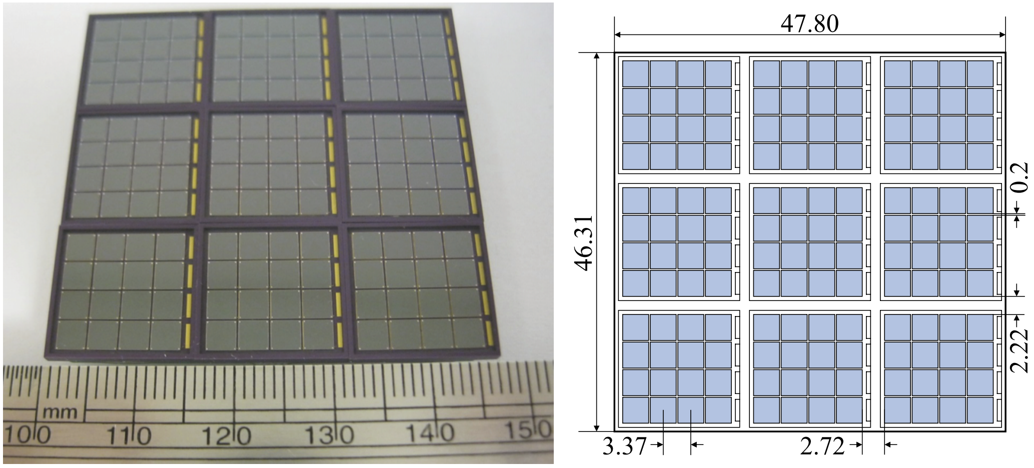

Fig. 1. Photograph of Matrix9 detector head (left) and dimensions in mm (right).

biased at the same bias voltage. This setup, in which only part of the Matrix9 active area is coupled to scintillator, allows mispositioning of events into adjacent SiPM arrays due to triggering errors to be quantified. Mispositioning of events can be caused by the readout logic (see Secs. 2.B and 2.C.5).[21] The LSO arrays, detector heads, and front-end electronics boards were placed in an aluminum light-tight black box connected to electrical ground for light and electromagnetic shielding. The temperature inside the box was controlled using an air-jet crystal cooler (FTS Systems, Inc., Stone Ridge, NY) and the temperature of the detector head was measured by the integrated digital temperature sensor of the Matrix9, which is located under the detector head. The temperature sensor has a granularity of 0.0625 °C.

A single LSO array and Matrix9 detector was used to measure the noise, signal, SNR, flood histogram quality, and array trigger errors. For these measurements, a 100 μCi ^{68}Ge point source was used to irradiate the crystals and was placed 20 mm above the front end of the LSO array. The count rate for the measurements was ~20 000 counts/s. For the timing resolution measurements, the source was located centrally between two Matrix9 detectors, with a center-to-center distance of 80 mm. For the count rate measurements, an 8×8 polished LYSO array (with a pitch of 1.5 mm and length 12 mm, separated by ESR reflector) was used.

2.B. Scrambled crosswire readout architecture

The Matrix9 detector head consists of 144 SiPM pixels. If each SiPM pixel were read out individually at least 144 electronic channels would be needed. To reduce the complexity of the readout electronics, and retain good performance, a multiplexing technique is used to read out the 144 SiPM pixels using only 25 electronic channels (Fig. 2). The 25 electronic channels consist of 9 cathode signals and 16 anode signals. In the scrambled crosswire readout method the 16 cathode pixel signals, one from each of the 16 SiPM pixels in a SiPM array, are summed to form one SiPM array signal. These 9 array signals in a Matrix9 module are used to identify the SiPM array in which the light photons interacted. To determine the interaction position within a particular SiPM array, on the anode side of the detector readout the nine SiPM pixels with the same location within an array (e.g., the nine top left pixels) are summed together to form 16 pixel signals. Consequently, when a particular SiPM pixel fires, a pulse occurs on its corresponding array signal channel and the corresponding pixel signal channel; by analyzing the 9 array signals and the 16 pixel signals the SiPM pixel that fired can be determined. This technique involves setting two energy thresholds, the array trigger threshold and the pixel trigger threshold. These are studied in Sec. 2.C.5.

Each array and pixel signal from the detector head was passed through a preamplifier and then a comparator. Each preamplified pixel signal was also fed to a slow shaper providing CR-RC (Ref. 2) shaping with a shaping time of 500 ns, allowing the gamma energy deposited in the LSO/LYSO scintillator to be accurately determined. The output of the slow shaper was connected to a 12-bit serial ADC. The peak value of the shaped signal was digitized and used as the pixel signal amplitude.[21]

Timing information was acquired from the first pulse transition within the 16 pixel signals by automatically latching a free-running time-to-digital converter (TDC) value implemented inside the FPGA to record the pulse transition time, which was then taken to be the interaction time. The pulse transitions are generated by 16 leading edging discriminators and a common low level threshold. The TDC is a 16-bit counter with a timing resolution of 0.5 ns.[21]

2.C. Detector performance measurements

2.C.1. *Signal to noise and energy resolution*

To study the dependence of bias voltage and temperature on detector performance, signal to noise measurements were performed. As there is no internal trigger in the Matrix9 electronic system the noise of the detector was acquired by setting the array and pixel threshold both to be zero, triggering the system by noise. The noise data (including the noise from the Matrix9 detector head and the readout electronics) were acquired with the crystal array coupled to the detector head and radiation source present. Measurements were carried out at the same set of bias voltages as the signal data. Linear interpolation of the data from each of the 16 pixel signal channels individually allows the 16 full widths at half maximum (FWHMs) and 16 peak positions of the noise distribution to be obtained. The average of these 16 FWHMs was treated as the detector noise, which includes the detector head noise and noise from the electronic readout. The voltage at the peak of the noise distribution from each pixel was treated as the

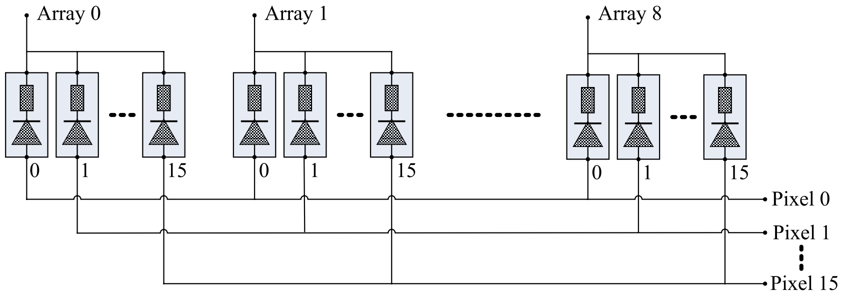

FIG. 2. Schematic of scrambled crosswire readout technique.

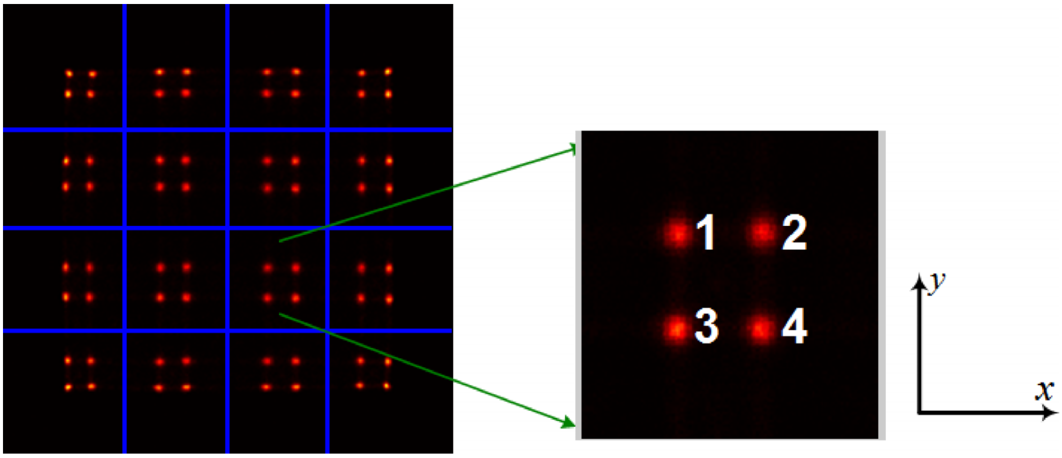

FIG. 3. Figure illustrating how flood histogram quality metric was computed. See text for details.

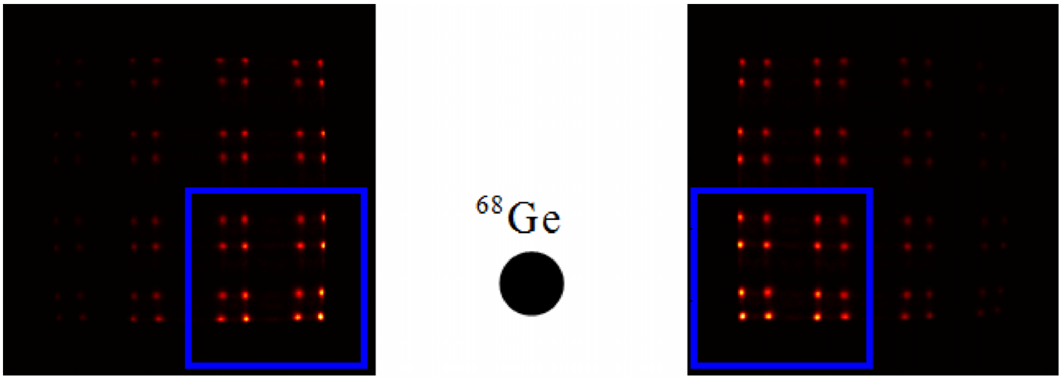

FIG. 4. Illustration of the measurement geometry for timing. Distance and object size are not to scale.

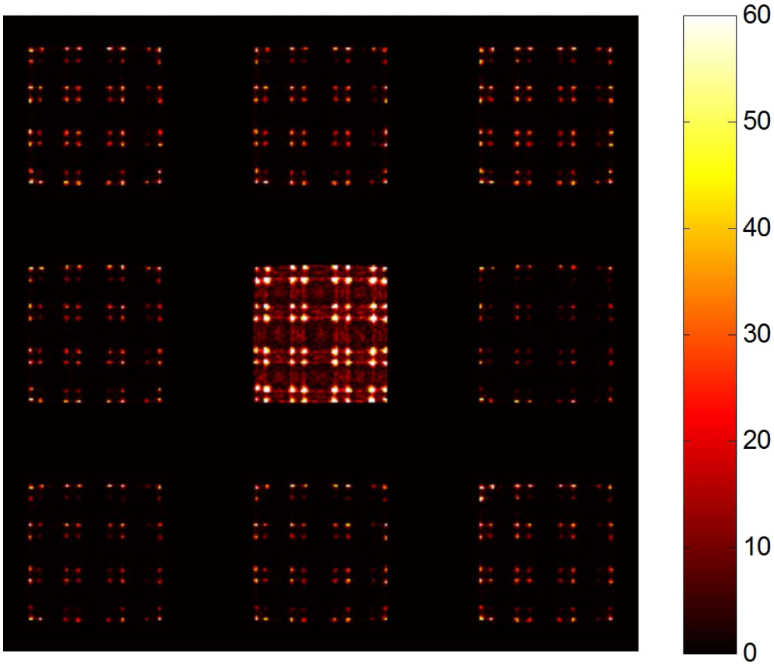

FIG. 5. Ghost floods appear due to triggering errors when the array threshold is not set high enough. In this example, the crystal array only covered the center SiPM array; events appearing in the surrounding eight SiPM arrays are considered trigger errors.

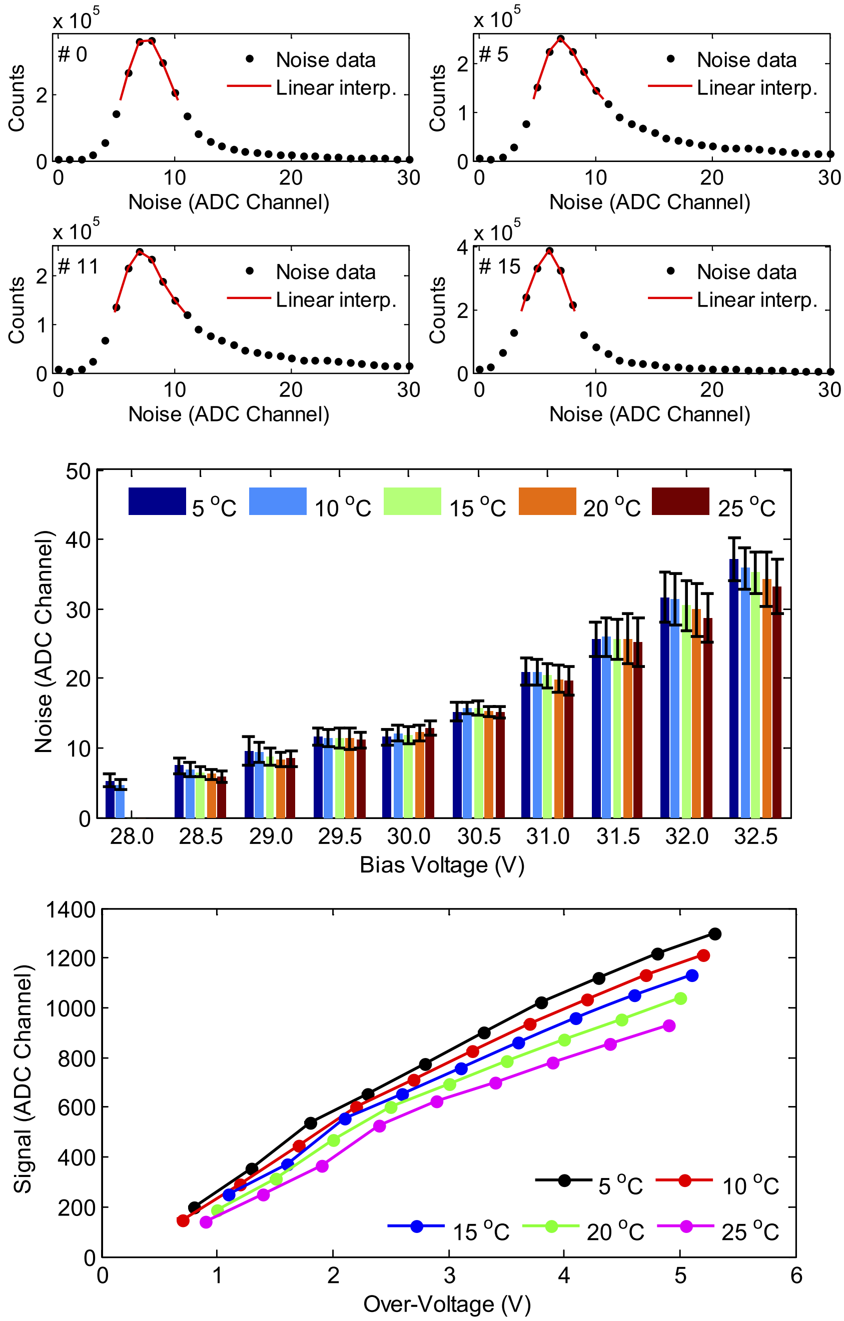

Fig. 6. (Top) noise distribution of four representative SiPM pixels (0, 5, 11, and 15). (Middle) noise and (bottom) signal versus temperature and bias voltage. The error bars in the middle figure are the standard deviation of the noise from the 16 SiPM elements, and in the bottom figure are the Gaussian fitting error.

signal offset of that corresponding pixel channel. The signal of the detector was measured as the 511 keV photopeak voltage in the energy histogram (obtained using the summed signal of all SiPM pixels) and was obtained by setting the array threshold and the pixel threshold both to 0.3 V. The signal amplitude was also corrected by subtracting the channel offset. The SNR was defined as the ratio of the 511 keV photopeak voltage to the detector noise voltage. The method used to obtain SNR here is slightly different from the approach we have used previously,[38,39] as the noise is averaged over 16 pixels. The energy resolution was taken as the % FWHM of the 511 keV photopeak. The saturation of the SiPM was not corrected because we found it did not greatly impact the results.

2.C.2. *Flood histograms*

Detector flood histograms were also calculated from the data acquired during the detector signal measurements. Four different methods were used to calculate the gamma photon interaction position based on center of gravity logic and compared:

- M1: *All energies method*—the signal from all 16 pixels in a SiPM array are used to calculate the interaction position.

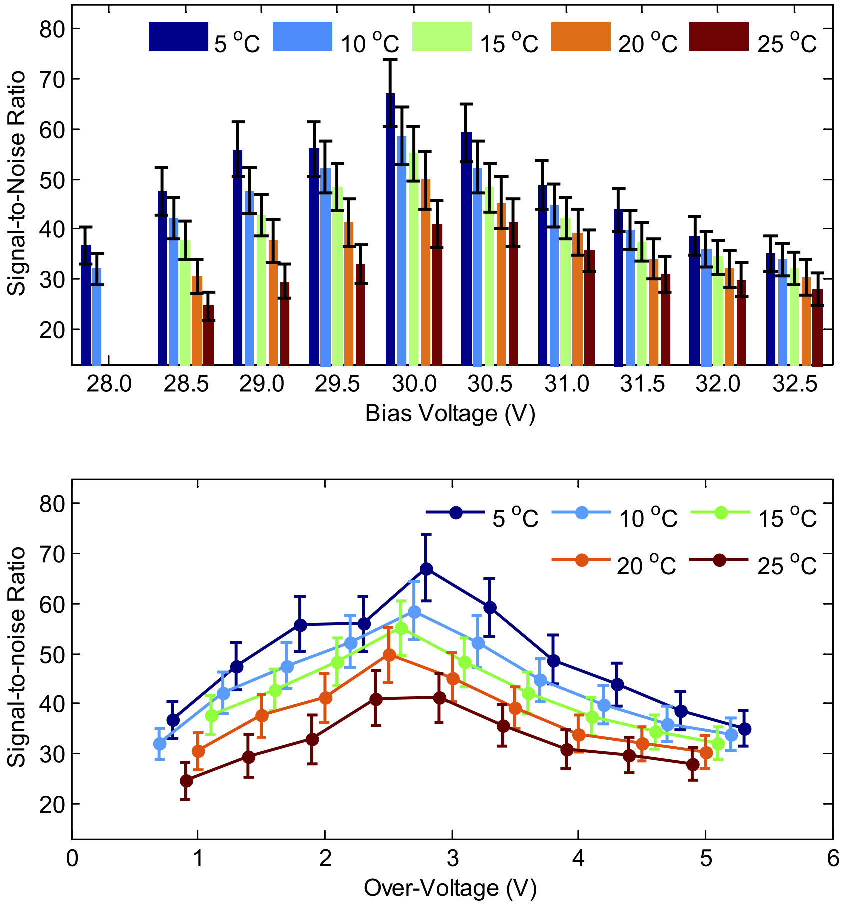

Fig. 7. SNR versus temperature and (top) bias voltage, (bottom) overvoltage.

- M2: *All energies method with offset calibration*—the offset measured above was subtracted from each signal prior to calculating the position.
- M3: *Region of interest (ROI) method*—uses the local 9 pixels—the pixel with the maximum signal and its eight surrounding pixels. If the pixel with the maximum value is an edge or corner pixel, the missing surrounding pixels are filled with zeros.
- M4: *ROI method with offset calibration*.

For the methods involving "offset calibration," the signal offset was first subtracted from the signal, if the subtracted signal was smaller than half of the FWHM measured from the noise distribution for that pixel, the signal was set to 0.

To quantitatively compare the flood histogram quality, a flood histogram quality metric was derived from methods in the literature[39] and adapted to the characteristics of the Matrix9 detector flood histogram. Figure 3 shows a flood histogram of the 8×8 LSO array. The flood histogram shows that due to the geometry of the crystal and SiPM array, the 64 crystals are grouped into sixteen 4-crystal groups, which represent the most difficult crystals to be separated and could be seen as a worst-case-estimate of the separation capability. For optimal crystal separation in each 4-crystal group, the distance between two adjacent crystals should be as large as possible and the spot size of the crystals as narrow as possible. This led us to calculate a flood histogram quality parameter k_i for the ith crystal group using the following formula:

$$k_i = \frac{1}{4}\left(\frac{x_2-x_1}{(w_{x2}+w_{x1})/2}+\frac{x_4-x_3}{(w_{x4}+w_{x3})/2}+\frac{y_1-y_3}{(w_{y1}+w_{y3})/2}+\frac{y_2-y_4}{(w_{y2}+w_{y4})/2}\right), \qquad (1)$$

where w_{xj} and w_{yj} are the FWHMs of the x and y projections of the flood histogram of the jth crystal in ith 4-crystal group, and x_j and y_j are the centroids of the x and y projections of the flood histogram of the jth crystal, as shown in Fig. 3. The mean value of the 16 k_i's, representing an average ratio of the crystal profile separation to the FWHM of the profiles, was used as the flood histogram quality metric and the standard deviation was used as the error range of k. Here, a larger value of k indicates better flood histogram quality.

2.C.3. Timing measurements

The timing resolution was measured at several temperatures using the optimal bias voltage determined by the SNR and flood histogram quality metrics. Different bias voltages were used at different temperatures (T) to maintain the same overvoltage. The bias voltage was calculated as $(29.7+0.02\times T)$ volts as the breakdown voltage is known to increase

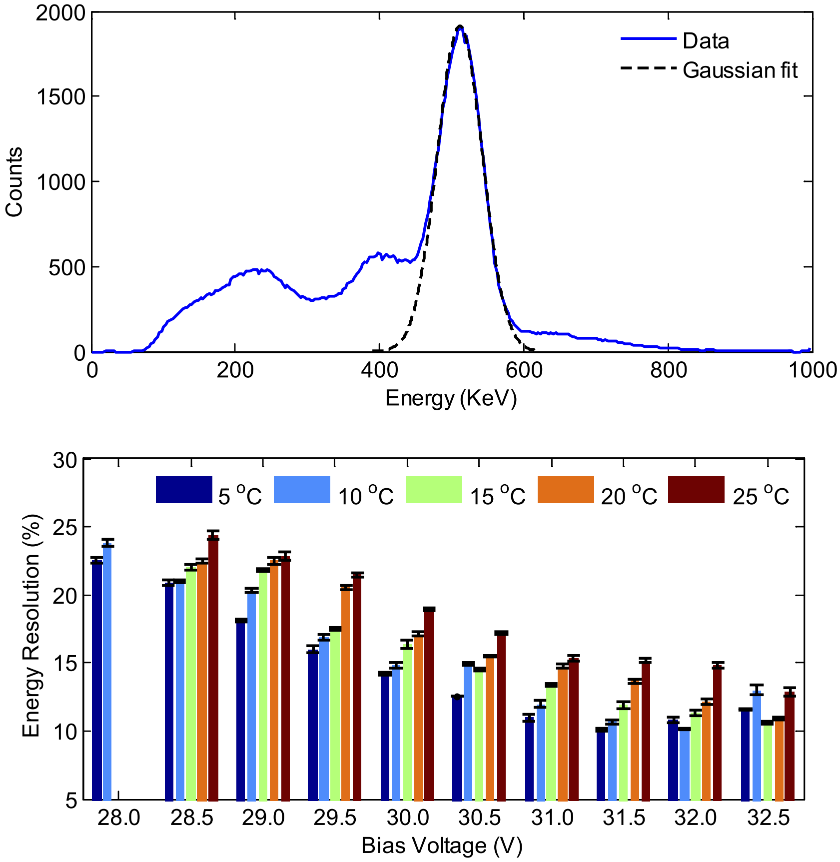

Fig. 8. (Top) energy spectra obtained at a bias voltage of 30.0 V and 5 °C and (bottom) energy resolution versus temperature and bias voltage.

linearly with temperature (~0.02 V/°C).[21] To simplify the timing resolution measurement, we used the symmetry of the SiPM detector array and crystal array to calculate the timing resolution for 16 crystals in each crystal array, as shown by the blue rectangles in Fig. 4. These 16 crystals represent all possible light sharing scenarios between crystal and SiPM array. The Matrix9 uses a leading edge discriminator (LED) to pick-off the timing information from the pixel signal. The time walk of the LED drastically degrades the attainable timing resolution and must be corrected. Using the relationship between the time pick-off and the corresponding energy of pixel (from which time information was picked up), a correction lookup table (LUT) can be created and applied to the timing data.[40]

2.C.4. *Effect of count rate*

To investigate the effect of the count rate and pile up on the detector performance (signal amplitude, flood histogram, and energy resolution), a $14\times14\times3$ mm^3 phantom filled with an initial activity of 10.8 mCi ^{18}F was placed 20 mm above the crystal surface. Count rate and signal data were acquired every hour for 30 h. The count rate caused by the LYSO background was also measured by removing the ^{18}F source. Count rate data were obtained with the array threshold set to 0.3 V and pixel threshold set to 0.1 V, and the signal amplitude data were obtained by setting both the array threshold and pixel threshold to 0.3 V. All the measurements were done at a bias voltage of 30.0 V and a temperature of 5 °C. Energy resolution and flood histogram quality were calculated using the methods described in Secs. 2.C.1 and 2.C.2.

2.C.5. *Array trigger errors*

For the above measurements (noise, signal, SNR, flood histogram, and timing resolution) events were selected from the central SiPM array, as determined by the array trigger, because the LSO array was only located over the central SiPM array and the other 8 SiPM arrays were covered with black paper. However, in these measurements, we noted that the array trigger did not always correspond to the central SiPM array. When this happens, the γ photon interaction position will be mispositioned to another SiPM array. These mispositioned γ photons are not just dark noise—as "ghost" flood images appear in the other eight SiPM arrays, as shown in Fig. 5. The Matrix9 uses the first arriving pixel trigger to trigger the data acquisition system to digitize the 16 pixel signals, and the first arriving array signal to decide which SiPM array these 16 pixels signals come from. Hence if the array threshold is too low, the array trigger may be triggered by noise and therefore will not relate to the actual array in which the event occurred. The array trigger error is related to the array threshold and was

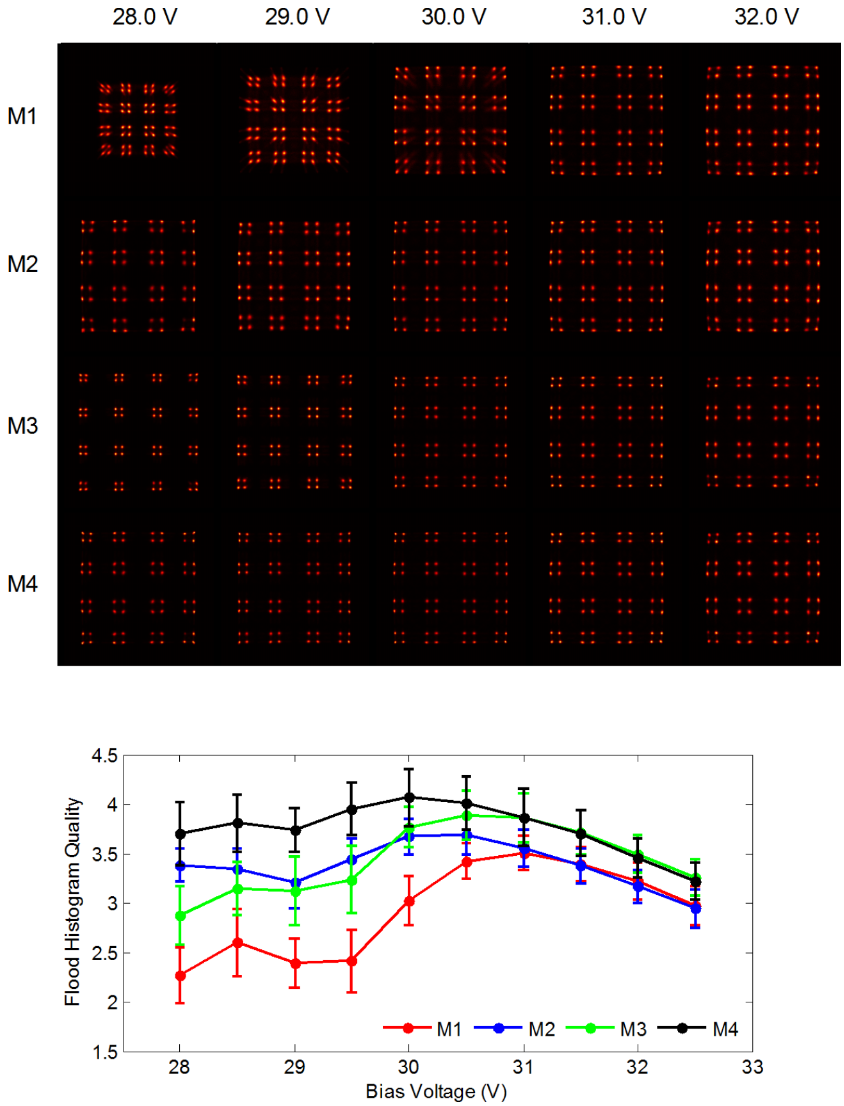

Fig. 9. (Top) flood histogram and (bottom) flood histogram quality metric using different positioning methods at different bias voltages. All measurements were acquired at 5 °C.

defined by the following function:

$$\text{array\_trigger\_error} = \frac{\sum_{i=0}^{8} n_i - n_4}{\sum_{i=0}^{8} n_i}\%, \qquad (2)$$

where $i = 0,\ldots,8$ is the SiPM array identification number, and n_i is the number of events assigned to SiPM array i. The array trigger error was measured at the same overvoltage for five different temperatures. The bias voltage applied at a given temperature T was $(29.7+0.02\times T)$ V. At each temperature, measurements were obtained at a fixed pixel threshold of 0.3 V (corresponding to ~150 keV) and different array thresholds, from 0 to 0.75 V in 0.05 V intervals, and also with an energy threshold applied during postprocessing of the data.

3. RESULTS

3.A. Detector noise and signal amplitude

The noise and the 511 keV photopeak signal amplitudes from the detector are plotted against bias voltage and temperature in Fig. 6. At the lowest bias voltage of 28.0 V, meaningful data could only be obtained at temperatures at or below 10 °C. The noise increases more rapidly at higher bias voltage than at lower bias voltage, meaning SiPM pixel dark noise does not increase linearly with voltage.[18,28,37,39] However, unlike the position-sensitive silicon photomultipliers (PS-SSPM), noise is not reduced significantly at lower temperature for a fixed bias voltage, which was significantly reduced for the PS-SSPM.[28] At a given bias voltage, the noise at lower temperatures is slightly larger than that at higher temperature, which is mainly due to the decrease of the breakdown voltage with decreasing temperature. The signal increases with bias voltage, but the slope decreases as the bias voltage increases.

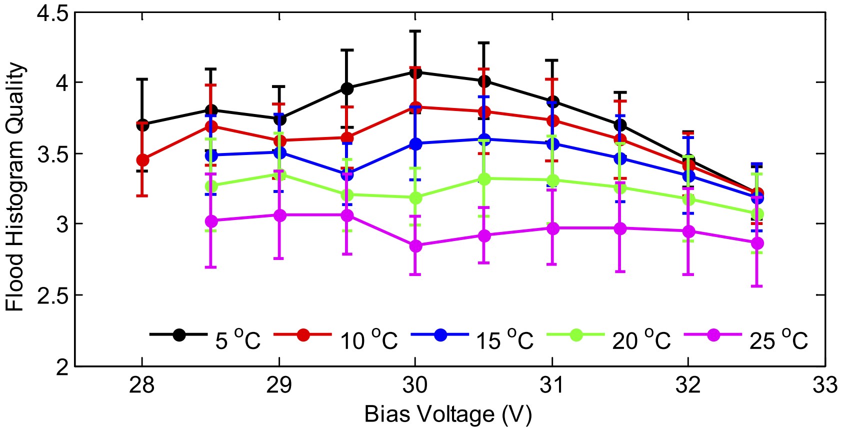

FIG. 10. Flood histogram quality metric based on ROI with offset calibration method at different bias voltages and different temperatures.

3.B. Signal-to-noise ratio

The SNR at different bias voltages and overvoltages, as a function of temperature, is shown in Fig. 7. The SNR first increased and then decreased with increasing bias voltage, due to the variation of the noise and signal shown in Fig. 6. Higher SNR was achieved at lower temperatures. For all temperatures the best SNR was obtained at a bias voltage between 30.0 and 30.5 V. Higher overvoltage conditions, such as increased bias or decreased temperature at a fixed bias result in higher SNR. This holds true up to approximately 30.0 V where the increase in dark noise begins to impact the SNR measurement.

3.C. Energy resolution

The global energy spectrum and energy resolution versus bias voltage and temperature is shown in Fig. 8. At a fixed bias voltage, the energy resolution improves with lower temperature. The measured energy resolution was 14.2% ± 0.1% at a bias voltage of 30.0 V (the optimal bias voltage for SNR from Fig. 7) and at a temperature of 5 °C. At higher bias voltages and lower temperatures the energy resolution becomes artificially good because of the nonlinearity of the SiPM (saturation effects were not corrected).

3.D. Flood histogram quality

Figure 9 shows the flood histogram (top) and flood histogram quality metric (bottom) obtained for different bias voltages at a fixed temperature of 5 °C using the four different position calculation methods. The best flood histogram quality was achieved using method M4, the "ROI with offset calibration" method. This gave the best and most consistent results, as the signal offset has been subtracted and the noise has been minimized by only using a local cluster of SiPM pixels for positioning (9 SiPM pixels instead of 16 SiPM pixels). The best flood histogram quality was achieved for bias voltages between 30.0 and 31.0 V for all four methods. The flood histograms also clearly show that an LSO array with a pitch of 1.5 mm can be resolved, and the separation suggests that smaller crystals (~1 mm pitch or smaller) might also be resolved. Figure 9 (bottom) also indicates that offset calibration must be performed when the signal is small, as the offset calibration method dramatically improves the flood histogram quality.

Figure 10 shows the flood histogram quality metric at different bias voltages and different temperatures using the ROI with offset calibration method. The flood histogram quality first increased and then decreased slightly as the bias voltage increased, which is consistent with the SNR results shown in Fig. 7. The best flood histogram quality was achieved at a temperature of 5 °C.

To further investigate the crystal identification ability of the Matrix9 detector, a 8 × 8 polished LYSO array (pitch 1.5 mm, length 12 mm), a 9×9 polished LYSO array (pitch 1.35 mm, length 12 mm), and a 10×10 polished LSO array (pitch 1.0 mm, length 10 mm) all using ESR as the intercrystal reflector, were also studied. These three crystal arrays were coupled to the detector head sequentially and also simultaneously (on SiPM section nos. 3, 4, and 5). The goal of the simultaneous measurement was to evaluate the ability of the scrambled crosswire readout method to decode multiple scintillator arrays at the same time. The corresponding flood histograms, calculated using method M4, are shown in Fig. 11. All the crystal elements in the three arrays were clearly resolved except some edge crystals in the 1.35 mm pitch LYSO array. In this case, the two outer rows/columns of crystals are both almost entirely coupled to the same SiPM pixels and it is difficult to separate them, as there is very limited light sharing.[33] A light guide may help to better separate the outer crystals but was not considered in this work. For the 1.0 mm pitch array all the crystals are resolved; however, this array does not extend to the very edges of the active area of the SiPM array. Nonetheless, it illustrates the potential to resolve small crystal elements.

To quantitatively compare the results obtained from sequentially and simultaneously coupling the crystal arrays to the detector head, the flood histogram quality and energy resolution were measured and are listed in Table I. The flood histogram quality was calculated by taking the average distance/width for every two adjacent crystals in both x and y direction, in order to compare flood histograms of the three crystals. Importantly,

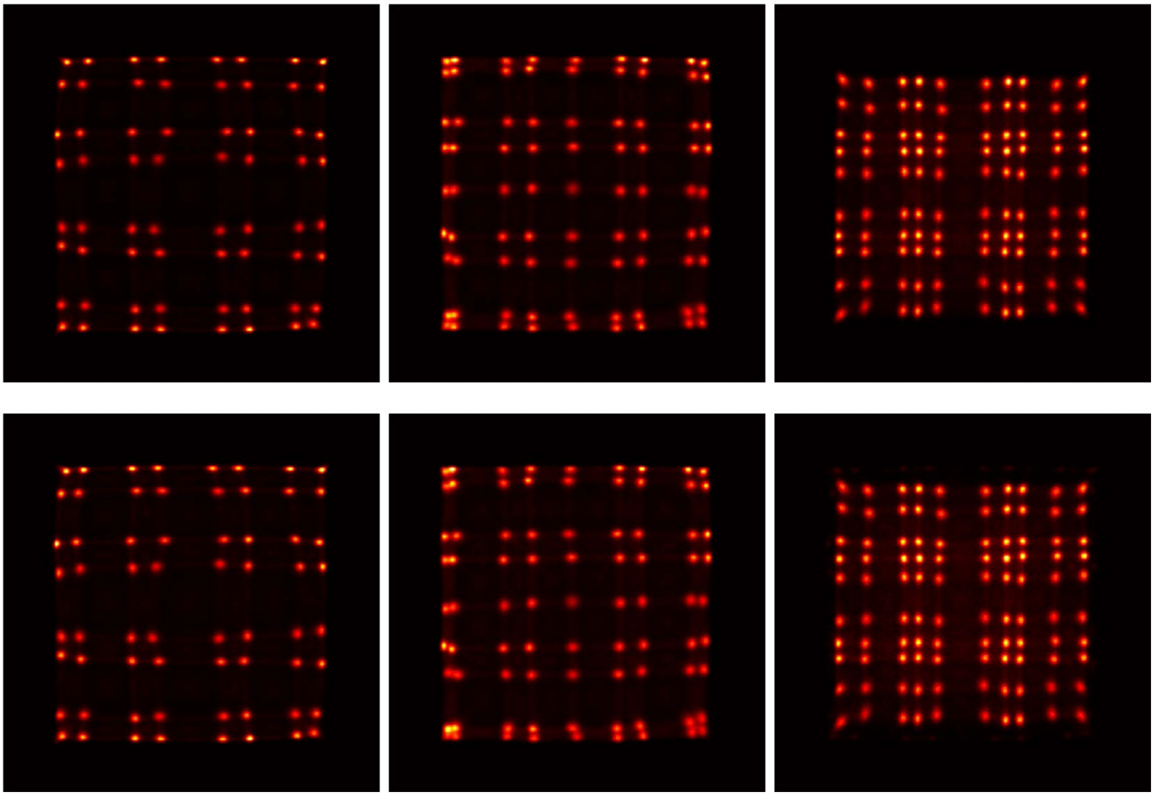

FIG. 11. Flood histograms of (left column) pitch 1.5 mm, (middle column) pitch 1.35 mm, and (right column) pitch 1.0 mm LYSO or LSO crystal arrays. Flood histograms shown in top row and bottom row were obtained by coupling crystal arrays sequentially and simultaneously.

the detector performance did not deteriorate when coupling more than one crystal array to the Matrix9 detector head simultaneously, supporting the ability to ultimately populate it with nine crystal arrays at the same time to make a full detector module.

3.E. Timing resolution

Figure 12 illustrates the measured coincidence timing spectrum at a temperature of 5 °C (top) and timing resolution at different temperatures (bottom). The red and blue curves indicate the results from the raw data and from data corrected using "LED time walk calibration," respectively. The solid and dashed curves in Fig. 12 (bottom) indicate the timing resolution for each method with an open energy window (lower cut-off is determined by the 0.3 V array threshold applied to the trigger threshold setting, which is around ~150 keV) and a 400–650 keV energy window applied to each crystal of the 16 selected crystals in the crystal array. The results, which are the average of all 256 (16×16) possible crystal pair timing spectra, show that the LED time walk calibration provided a significant improvement in the timing resolution. Figure 12 (bottom) indicates that using a narrow energy window improves the timing resolution, as the amplitude range of events is restricted, thus reducing time walk effects. A slightly better timing resolution can be achieved at lower temperature, but the improvement is rather limited, especially after using the time walk calibration and using an energy window.

3.F. Count rate effects

Figure 13 shows the flood histogram, and Fig. 14 shows the flood histogram quality, energy resolution, and signal amplitude (511 keV photopeak) obtained at different count rates. It is obvious that in very high count rate conditions, the flood histogram and energy resolution were both degraded. The

TABLE I. Comparison of flood histogram quality metric and energy resolution.

	Flood histogram quality		Energy resolution (%)	
Crystal array (pitch size/mm)	Sequentially	Simultaneously	Sequentially	Simultaneously
1.5	4.4 ± 0.5	4.3 ± 0.5	14.4 ± 0.7	14.8 ± 0.8
1.35	3.2 ± 0.7	3.1 ± 0.8	14.7 ± 0.7	15.1 ± 0.9
1.0	2.9 ± 0.3	2.8 ± 0.3	15.5 ± 0.6	16.0 ± 0.7

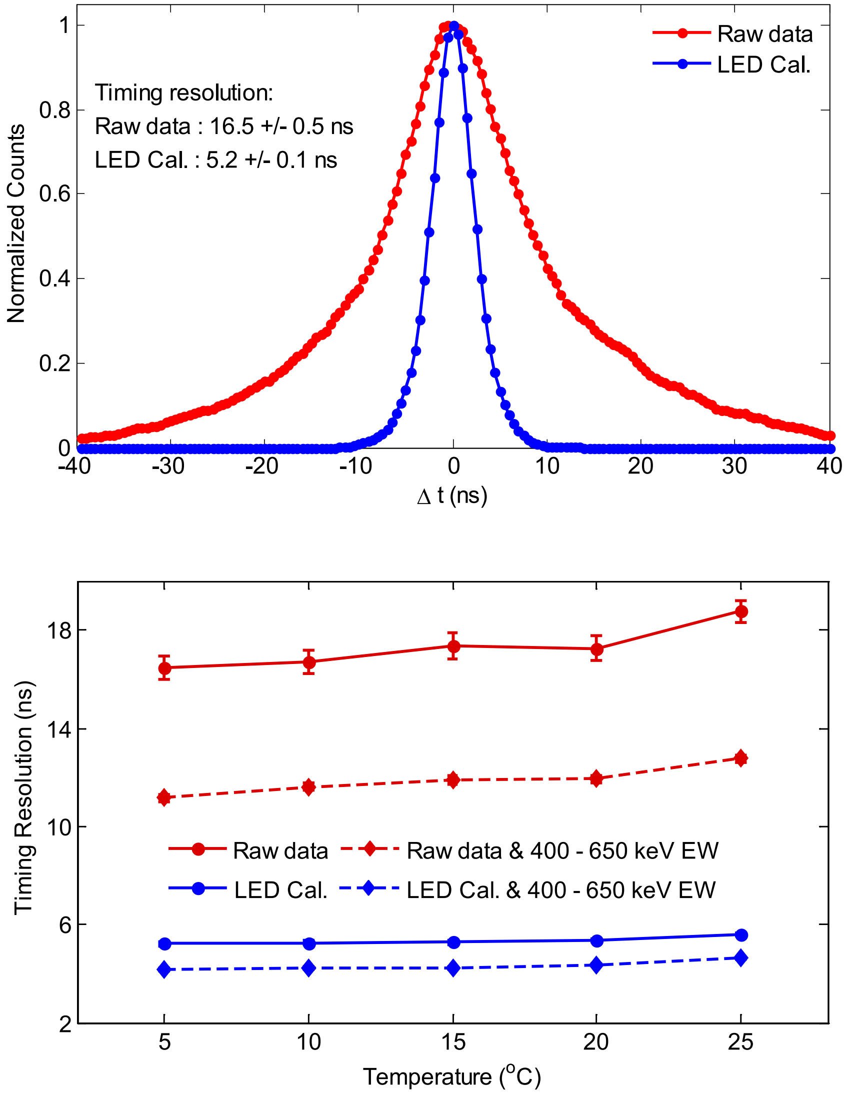

FIG. 12. (Top) timing spectra at 5 °C and (bottom) timing resolution at different temperatures. The solid lines correspond to an open energy window (~150 keV lower cut off) and the dashed lines to a 400–650 keV threshold.

signal amplitude decreased with increasing count rate, mainly due to the partial charging of the microcells at high count rate. The microcells in the Matrix9 SiPMs have a typical recovery time of 130 ns.[37] Under high count rate conditions, the microcells are not fully charged before the next discharge process; hence, the signal amplitude is decreased. This phenomenon, as well as pulse pileup, also degraded the flood histogram and energy resolution. The data show that count rates of ~100 000 counts/s can be maintained without any performance degradation.

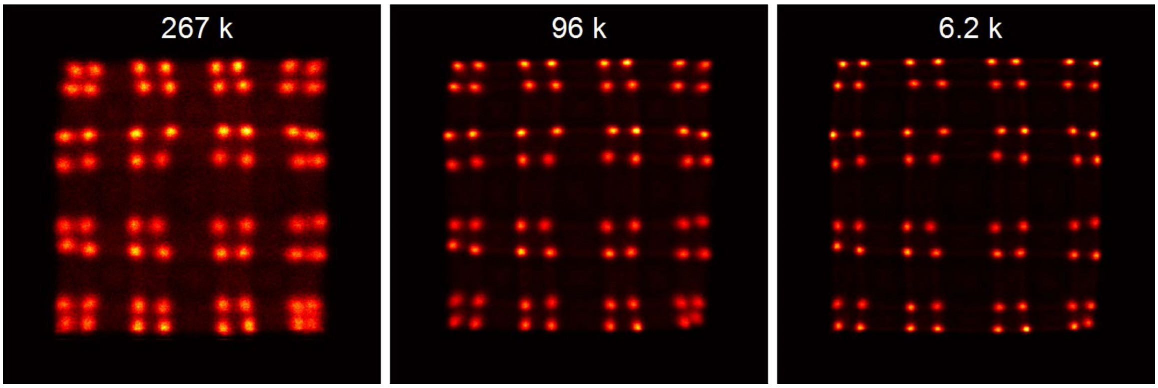

FIG. 13. Flood histogram obtained at different count rates.

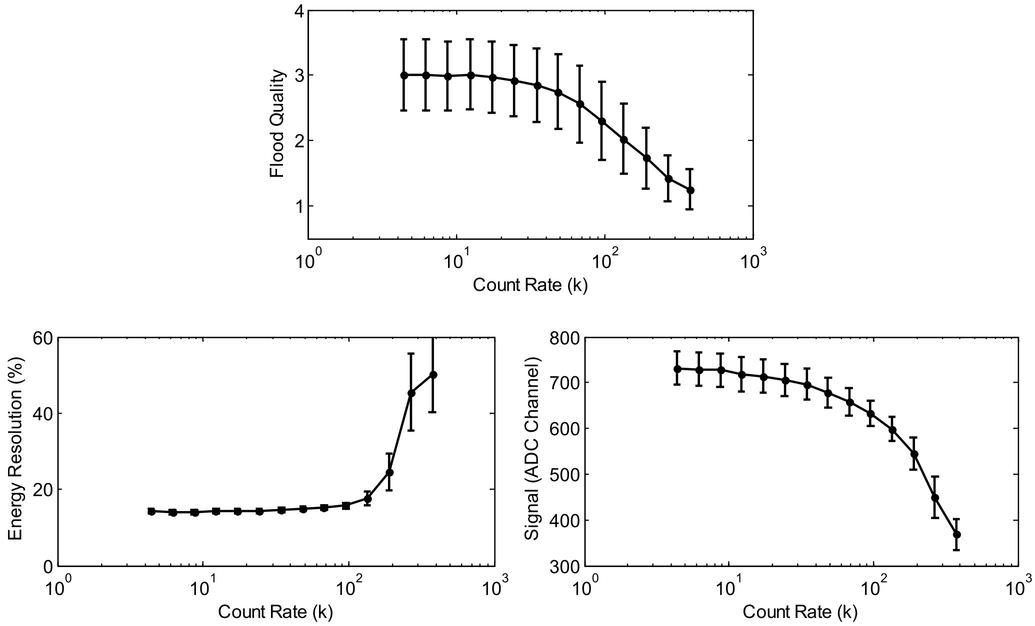

FIG. 14. (Top) flood histogram quality, (bottom left) energy resolution, and (bottom right) signal amplitude versus count rate.

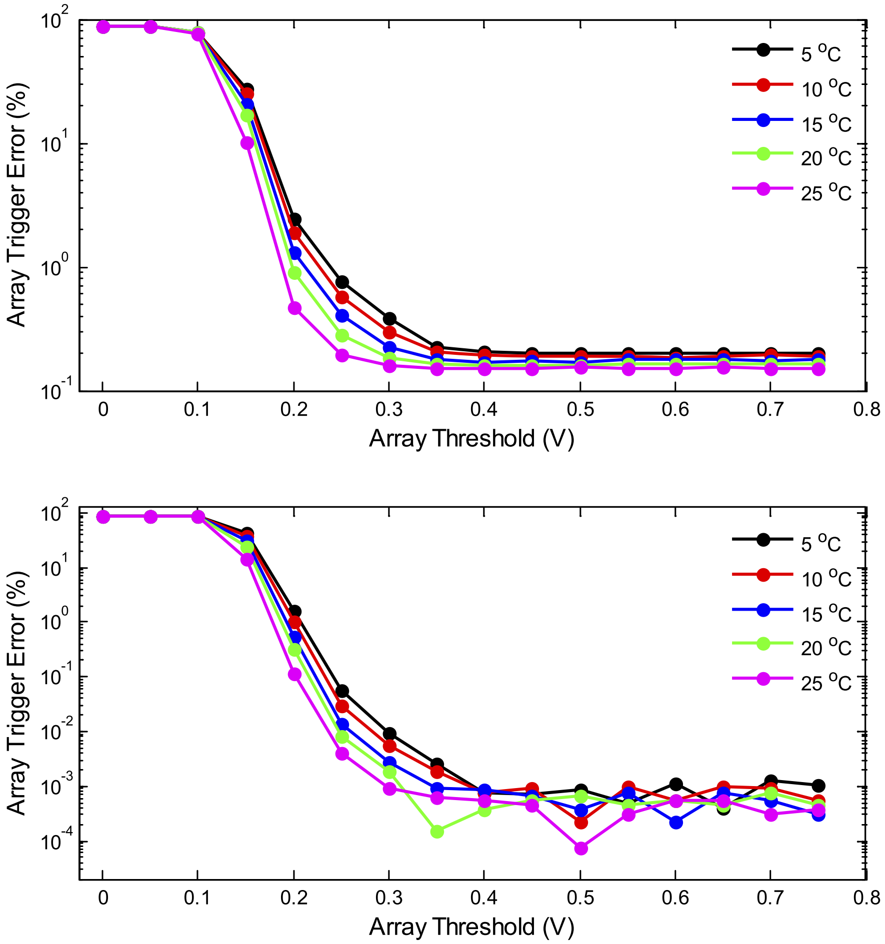

FIG. 15. Array trigger error versus temperature and array threshold level with (top) a wide open energy window and (bottom) a 400–650 keV energy window. Note that vertical scales are logarithmic and are not the same for the two plots.

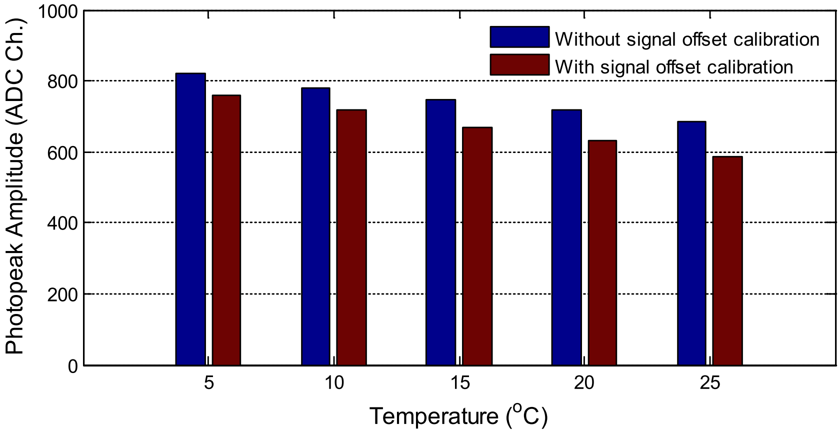

FIG. 16. 511 keV photopeak amplitude as a function of temperature for the same overvoltage. The photopeak amplitude still has some small dependence on temperature.

3.G. Array trigger errors

The Matrix9 has two online discriminators that can be set: the array threshold and pixel threshold. The array threshold and the pixel threshold function similarly to a lower level discriminator in an energy spectrum while the array threshold is also used to determine which of the nine SiPM arrays has fired. The array trigger error was measured as the array threshold level was changed (the pixel threshold was fixed at 0.3 V) and is plotted in Fig. 15. As expected, the array trigger error first decreases and then becomes rather constant as the array threshold level is increased. When the array threshold is higher than the noise of the SiPM array, the probability of having a trigger from the SiPM array not coupled to the crystal array is reduced. With the array threshold greater than 0.3 V, the array trigger error ratio is ~0.1% [Fig. 15 (top)]. Using a 400–650 keV energy window to filter out the low energy events does decrease the array trigger error ratio, but it only has a significant effect when the array threshold level is higher than 0.2 V. With an energy threshold set in post processing of the data there is practically no array trigger error when the array threshold is higher than 0.3 V [Fig. 15 (bottom)]. The fluctuations seen in Fig. 15 (bottom) are due to the stochastic nature of the measurement and the very low number of trigger errors that occur in this regime.

We also measured the array trigger error ratio at a fixed 0.3 V array threshold for different pixel thresholds ranging from 0 to 0.65 V, in 0.05 V increments. The array trigger error did not change significantly by increasing the pixel threshold level (results not shown), which implies that the array trigger error is mainly dominated by the array threshold level and not the pixel threshold level. The reason why the array trigger error was not significantly affected by the pixel threshold is due to the trigger principles of the Matrix9 electronics system, which uses the pixel signal to trigger the system and both the pixel signal and the array signal to validate the event. If the pixel threshold is low and the system was triggered by noise, there will not be a valid array signal (array threshold is above noise) and these noise events will be discarded.[21]

The array trigger error was evaluated at the same overvoltage; hence, the array trigger error at lower temperatures was expected to be smaller than that at higher temperatures, as the noise of the SiPM is lower. But, we in fact observed a slight increase in the array trigger error ratio. The reason for this may be that the bias voltages were changed according to the expected rate of 0.02 V/°C in order to keep the SiPM at the same overvoltage, however, each device may not vary exactly according to this relationship. Some residual difference in the 511 keV photopeak amplitude, as shown in Fig. 16, was still observed. At lower temperatures, the signal amplitude is a little larger, which means the gain is higher, hence the noise is higher, causing a larger array trigger error.

4. DISCUSSION AND CONCLUSIONS

This study presented a detailed performance test of the large-area Matrix9 SiPM detector in the context of its possible application for small-animal PET. We measured the SNR, flood histogram quality, energy resolution, timing resolution, count rate effect, and the array trigger error ratio. Both the noise and signal increase with increasing bias voltage, but only the signal amplitude is significantly affected by temperature variations. SNR results and flood histogram quality show that the overall best performance was achieved when a ~30.0 V working bias voltage was applied and better results were obtained at lower temperature. The energy resolution at 5 °C and a bias voltage of 30.0 V was 14.2 ± 0.1%. We believe that even better SNR and flood histogram quality can be obtained at temperatures lower than 5 °C, but these were not studied here, because our goal is to implement this detector at a system level with modest and readily achievable levels of cooling.

To obtain the best flood histogram quality, a ROI with offset calibration position calculation method was introduced in this paper. This method considers only nine local pixels to compute the γ interaction position and gave the best and most robust result at different bias voltages compared to the other methods. Using this technique, individual crystals in the LSO array with a pitch of 1.5 mm could be clearly resolved and the results suggested that crystal arrays with smaller pitch could be resolved as well. This was confirmed by tests on a 9×9 polished LYSO array (pitch 1.35 mm) and a 10×10 polished LSO array (pitch 1.0 mm).

With proper timing calibration, a 5.2 ns and a 4.2 ns timing resolution was achieved at 5 °C based on two Matrix9 detectors with a wide-open energy window and a 400–650 keV energy window, respectively. These values are compatible with most small-animal PET applications. The array trigger error, which is an inherent problem of the scrambled crosswire readout technique, can be reduced by using an array threshold above 0.3 V. If an energy window is used, the array trigger error ratio can be further reduced and will not degrade the flood histogram quality. This is therefore not an issue of any practical concern. We also demonstrated that the Matrix9 can read out multiple scintillator arrays simultaneously and that its electronics can handle event rates of 100 000 counts/s without any performance degradation.

Our proposed detector design will use nine individual LYSO or LSO arrays, each coupled to a single SiPM array, to prevent optical crosstalk between SiPM arrays. Assuming nine 8×8 arrays with a crystal pitch size of 1.5 mm, the fill factor will be 58.6%. We expect significant problems would occur if a single large area LSO array were used across the entire Matrix9 active area, as light sharing across SiPM arrays complicates the crosswire readout and position decoding if one crystal is coupled to more than one SiPM array.

Because the readout naturally allows the light distribution across all 16 pixels in the array to be sampled, we also will investigate the extraction of depth of interaction information using a single ended readout.[41] This could allow, without any increase in complexity, the use of longer crystals in the box geometry design, improving the sensitivity, while reducing spatial resolution degradation due to depth of interaction effects.

With these attractive performance parameters and ease of use, relatively simple high-resolution small-animal PET and PET/MRI scanners, or dedicated scanners for breast and brain imaging, could be based upon these modular Matrix9 large-area detectors and their associated electronics. In addition, further advances in SiPM array technology are rapidly occurring. New detectors with enhanced blue sensitivity to match the emission of LSO and LYSO,[3,4,15,42] lower dead space, and therefore improved PDE have recently become available and offer the prospect of even better performance. Once these advances get incorporated into large-area detectors with appropriate readout electronics, they will provide attractive opportunities for small-animal PET scanner designs.

ACKNOWLEDGMENTS

This work was funded in part by NIH Grant Nos. R01 CA134632 and R01 EB00993. The authors wish to thank Dr. Martin S. Judenhofer and Dr. Jian Zhou from the Department of Biomedical Engineering, University of California, Davis, for useful discussions.

[a] Author to whom correspondence should be addressed. Electronic mail: jwdu@ucdavis.edu

[1] T. Lewellen, "The challenge of detector designs for PET," Nucl. Med. Mol. Imaging **195**, 301–309 (2010).

[2] E. Roncali and S. R. Cherry, "Application of silicon photomultipliers to positron emission tomography," Ann. Biomed. Eng. **39**, 1358–1377 (2011).

[3] SensL, B-series fast, blue-sensitive silicon photomultiplier sensors, 2013, http://sensl.com/documentation/.

[4] A. Ferri, A. Gola, S. Serra, A. Tarolli, N. Zorzi, and C. Piemonte, "Performance of FBK high-density SiPM technology coupled to Ce:LYSO and Ce:GAGG for TOF-PET," Phys. Med. Biol. **59**, 869–880 (2014).

[5] E. Bolle *et al.*, "AX-PET: A novel PET concept with G-APD readout," Nucl. Instrum. Methods Phys. Res., Sect. A **695**, 129–134 (2012).

[6] K. Hong *et al.*, "A prototype MR insertable brain PET using tileable GAPD arrays," Med. Phys. **40**, 042503 (12pp.) (2013).

[7] K. Yamamoto, K. Yamamura, K. Sato, S. Kamakura, T. T. Ota, H. Suzuki, and S. Ohsuka, "Development of multi-pixel photon counter (MPPC)," in *IEEE Nuclear Science Symposium Conference Record (NSS/MIC)* (IEEE, 2007), pp. 1511–1515.

[8] A. Stewart, L. Wall, and C. Jackson, "Properties of silicon photon counting detectors and silicon photomultipliers," J. Mod. Opt. **56**, 240–252 (2009).

[9] T. Frach, G. Prescher, C. Degenhardt, R. de Gruyter, A. Schmitz, and R. Ballizany, "The digital silicon photomultiplier—Principle of operation and intrinsic detector performance," in *IEEE Nuclear Science Symposium Conference Record (NSS/MIC)* (IEEE, 2009), pp. 1959–1965.

[10] M. McClish, P. Dokhale, C. Christian, C. Stapels, E. Johnson, R. Robertson, and K. S. Shah, "Performance measurements of CMOS position sensitive solid-state photomultipliers," IEEE Trans. Nucl. Sci. **49**, 3269–3277 (2010).

[11] M. Mazzillo, G. Condorelli, D. Sanfilippo, G. Valvo, B. Carbone, A. Piana, G. Fallica, A. Ronzhin, M. Demarteau, S. Los, and E. Ramberg, "Timing performances of large area silicon photomultipliers fabricated at STMicroelectronics," IEEE Trans. Nucl. Sci. **57**, 2273–2279 (2010).

[12] P. Dokhale, R. Robertson, C. Stapels, J. Cristian, M. Kaul, S. Surti, J. Karp, P. Vaska, and K. S. Shah, "Continuous LYSO-SSPM array based PET detectors for clinical and small volume imaging studies," in *IEEE Nuclear Science Symposium Conference Record (NSS/MIC)* (IEEE, 2011), pp. 2350–2354.

[13] T. Kato, J. Kataoka, T. Nakamori, T. Miura, H. Matsuda, K. Sato, Y. Ishikawa, K. Yamamura, N. Kawabata, H. Ikeda, G. Sato, and K. Kamada, "Development of a large-area monolithic 4×4 MPPC array for a future PET scanner employing pixelized Ce:LYSO and Pr:LuAG crystals," Nucl. Instrum. Methods Phys. Res., Sect. A **638**, 83–91 (2011).

[14] V. Schulz, P. Dueppenbecker, C. W. Lerche, A. Gola, A. Ferri, A. Tarolli, and C. Piemonte, "Sensitivity encoded silicon photomultipliers (SeSPs): A novel detector design for uniform crystal identification," in *IEEE Nuclear Science Symposium Conference Record (NSS/MIC)* (IEEE, 2011), pp. 3027–3029.

[15] T. Pro, A. Ferri, A. Gola, N. Serra, A. Tarolli, N. Zorzi, and C. Piemonte, "New developments of near-UV SiPMs at FBK," IEEE Trans. Nucl. Sci. **60**, 2247–2253 (2013).

[16] K. Shimizu, H. Uchida, K. Sakai, M. Hirayanagi, S. Nakamura, and T. Omura, "Development of a multi-pixel photon counter module for positron emission tomography," IEEE Trans. Nucl. Sci. **60**, 1512–1517 (2013).

[17] A. Stolin, S. Majewski, G. Jaliparthi, and R. Raylman, "Construction and evaluation of a prototype high resolution, silicon photomultiplier-based, tandem positron emission tomography system," IEEE Trans. Nucl. Sci. **60**, 82–86 (2013).

[18] C. Piemonte, A. Ferri, A. Gola, T. Pro, N. Serra, A. Tatolli, and N. Zorzi, "Characterization of the first FBK high-density cell silicon photomultiplier technology," IEEE Trans. Nucl. Sci. **60**, 2567–2573 (2013).

[19] A. Kolb, C. Parl, F. Mantlik, C. C. Liu, E. Lorenz, D. Renker, and B. J. Pichler, "Development of a novel depth of interaction PET detector using highly multiplexed G-APD cross-strip encoding," Med. Phys. **41**, 081916 (9pp.) (2014).

[20] S. Adachi, S. Nakamura, M. Hirayanagi, H. Suzuki, T. Uchiyama, T. Baba, M. Watanabe, and T. Omura, "Development of MPPC array module," in *IEEE Nuclear Science Symposium Conference Record (NSS/MIC)* (IEEE, 2013), pp. 1–3.

[21] SensL Matrix9 system user manual, 2013, http://sensl.com/documentation/.

[22] S. Yamamoto, H. Watabe, and J. Hatazawa, "Performance comparison of Si-PM-based block detectors with different pixel sizes for an ultrahigh-resolution small-animal PET system," Phys. Med. Biol. **56**, N227–N236 (2011).

[23] H. Yoon, G. Ko, S. Kwon, C. Lee, M. Ito, I. Song, D. Lee, S. Hong, and J. Lee, "Initial results of simultaneous PET/MRI experiments with an MRI-

compatible silicon photomultiplier PET scanner," J. Nucl. Med. **53**, 608–614 (2012).

[24] T. Isobe, R. Yamada, K. Shimizu, A. Saito, K. Ote, K. Sakai, T. Moriya, H. Yamauchi, T. Omura, and M. Watanabe, "Development of a new brain PET scanner based on single event data acquisition," in *IEEE Nuclear Science Symposium Conference Record (NSS/MIC)* (IEEE, 2013), pp. 3540–3543.

[25] Y. Shao, X. Sun, K. Lan, C. Bircher, K. Lou, and Z. Deng, "Development of a prototype PET scanner with depth-of-interaction measurement using solid-state photomultiplier arrays and parallel readout electronics," Phys. Med. Biol. **59**, 1223–1238 (2014).

[26] P. Fischer and C. Piemonte, "Interpolating silicon photomultipliers," Nucl. Instrum. Methods Phys. Res., Sect. A **718**, 320–322 (2013).

[27] A. Gola, A. Ferri, A. Tarolli, N. Zorzi, and C. Piemonte, "A novel approach to position-sensitive silicon photomultipliers: First results," in *IEEE Nuclear Science Symposium Conference Record (NSS/MIC)* (IEEE, 2013), pp. 1–4.

[28] J. Schmall, J. Du, Y. Yang, P. Dokhale, M. McClish, K. Shah, and S. R. Cherry, "Comparison of large-area position-sensitive solid-state photomultipliers for small animal PET," Phys. Med. Biol. **57**, 8119–8134 (2012).

[29] C. L. Kim, D. McDaniel, and A. Ganin, "Time-of-flight PET detector based on multi-pixel photon counter and its challenges," IEEE Trans. Nucl. Sci. **58**, 3–8 (2011).

[30] J. Yeom, R. Vinke, V. Spanoudaki, K. Hong, and C. Levin, "Readout electronics and data acquisition of a positron emission tomography time-of-flight detector module with waveform digitizer," IEEE Trans. Nucl. Sci. **60**, 3735–3741 (2013).

[31] S. Yamamoto, M. Imaizumi, T. Watabe, H. Watabe, Y. Kanai, E. Shimosegawa, and J. Hatazawa, "Development of a Si-PM-based high-resolution PET system for small animals," Phys. Med. Biol. **56**, 5817–5831 (2010).

[32] T. Song, H. Wu, S. Komarov, S. Siegel, and Y. Tai, "A sub-millimeter resolution PET detector module using a multi-pixel photon counter array," Phys. Med. Biol. **55**, 2573–2587 (2011).

[33] C. J. Thompson and A. Goertzen, "Evaluation of a 16:3 signal multiplexer to acquire signals from a SiPM array with dual and single layer LYSO crystal blocks," IEEE Trans. Nucl. Sci. **58**, 2175–2180 (2011).

[34] E. Downie, X. Yang, and H. Peng, "Investigation of analog charge multiplexing schemes for SiPM based PET block detectors," Phys. Med. Biol. **58**, 3943–3964 (2013).

[35] C. Liu and A. Goertzen, "Multiplexing approaches for a 12 × 4 array of silicon photomultipliers," IEEE Trans. Nucl. Sci. **6**, 35–43 (2014).

[36] Z. Gu, R. Taschereau, N. T. Vu, H. Wang, D. L. Prout, R. W. Silverman, B. Bai, D. B. Stout, M. E. Phelps, and A. F. Chatziioannou, "NEMA NU-4 performance evaluation of PETbox4, a high sensitivity dedicated PET preclinical tomography," Phys. Med. Biol. **58**, 3791–3814 (2013).

[37] SensL, MicroSL silicon photomultiplier detectors datasheet, 2012, http://sensl.com/documentation/.

[38] Y. Yang, Y. Wu, R. Farrell, P. Dokhale, K. S. Shah, and S. R. Cherry, "Signal and noise properties of position-sensitive avalanche photodiodes," Phys. Med. Biol. **56**, 6327–6336 (2011).

[39] J. Du, J. Schmall, Y. Yang, K. Di, P. Dokhale, K. S. Shah, and S. R. Cherry, "A simple capacitive charge-division readout for position-sensitive solid-state photomultiplier array," IEEE Trans. Nucl. Sci. **60**, 3188–3197 (2013).

[40] J. Du, J. Schmall, M. Judenhofer, K. Di, Y. Yang, and S. R. Cherry, "A time-walk correction method for PET based on leading edge discriminators," in *IEEE Nuclear Science Symposium Conference Record (NSS/MIC) M09–1* (IEEE, 2013).

[41] Y. Yang, Y. Wu, and S. R. Cherry, "Investigation of depth of interaction encoding for a pixelated LSO array with a single multi-channel PMT," IEEE Trans. Nucl. Sci. **56**, 2594–2599 (2009).

[42] J. Yeom, R. Vinke, N. Pavlov, S. Bellis, L. Wall, K. O'Neill, C. Jackson, and C. S. Levin, "Fast timing silicon photomultipliers for scintillation detectors," IEEE Photonics Technol. Lett. **25**, 1309–1312 (2013).